Understanding conditions for the single electron regime in 28 nm FD-SOI quantum dots: Interpretation of experimental data with 3D quantum TCAD simulations

Ioanna Kriekouki, Félix Beaudoin, Pericles Philippopoulos, Chenyi Zhou, Julien Camirand-Lemyre, Sophie Rochette, Claude Rohrbacher, Salvador Mir, Manuel Barragan, Michel Pioro-Ladrière, et al.

Understanding conditions for the single electron regime in 28 nm FD-SOI quantum dots: interpretation of experimental data with 3D quantum TCAD simulations

Ioanna Kriekouki[1,2,3], Félix Beaudoin[4], Pericles Philippopoulos[4], Chenyi Zhou[4], Julien Camirand Lemyre [3], Sophie Rochette [3], Claude Rohrbacher[3], Salvador Mir[2], Manuel J. Barragan[2], Michel Pioro-Ladrière[3] and Philippe Galy[1]

1 STMicroelectronics, 850 rue Jean Monnet, 38920 Crolles, France
2 Université Grenoble Alpes, CNRS, Grenoble INP, TIMA, F-38000 Grenoble, France
3 Institut quantique, Université de Sherbrooke, 2500 Boulevard de l'Université, Sherbrooke QC J1K 2R1, Canada
4 Nanoacademic Technologies Inc., Suite 802, 666 rue Sherbrooke Ouest, Montréal QC H3A 1E7, Canada

1. Abstract

Single electrons trapped in quantum dots hosted in silicon nanostructures are a promising platform for the implementation of quantum technologies. In this study, we investigated the required conditions to attain the single-electron regime in an Ultra-Thin Body and Buried oxide (UTBB) Fully Depleted Silicon-On-Insulator (FD-SOI) quantum dot device fabricated using the standard manufacturing process of STMicroelectronics. The cryogenic temperature operation of the quantum dot device is simulated and analyzed using the 3D Quantum Technology Computer Aided Design (QTCAD) software developed by Nanoacademic Technologies, achieving convergence down to 1.4 K. We report here simulations exploring single-electron occupancy of a single side-gate activated corner quantum dot and compare them to experimental data collected from the measurements on a device with the same geometry.

2. Introduction

Quantum computers, which use quantum bits (qubits) as their building blocks, harness quantum mechanics in the hope of delivering disruptive advantages over a wide range of classical technologies. Quantum dots in semiconductor nanostructures offer a promising approach to implement physical qubits [1]. In this architecture, the quantum information is encoded into the spin of a single electron or hole confined in the dot.

Qubits based on silicon quantum dots in conventional CMOS technologies promise to enable reproducible, high-yield industrial manufacturing and co-integration with classical control hardware, two decisive steps toward scalability [2-6]. In addition, by decreasing turnaround times, industrial spin-qubit production allows for accelerated development of novel devices containing several qubits coupled to each other for large-scale, high-fidelity logical operations. A milestone towards a scalable qubit architecture is to develop a silicon-based qubit structure fabricated entirely using 300-mm wafer industrial manufacturing techniques.

We present here our work on the investigation of the performance of our quantum-dot device at very low temperatures fabricated using mass-production methods, based on the 28 nm Ultra-Thin Body and Buried oxide (UTBB) Fully Depleted Silicon-On-Insulator (FD-SOI) technology of STMicroelectronics which has already demonstrated functional operation at cryogenic temperatures [7-13]. Since FD-SOI remains a planar technology, the transition from conventional bulk processes is facilitated by the fact that many manufacturing methods can be adapted more easily, resulting in a less expensive and simpler fabrication process than the FinFET alternative [14]. In order to define a high-quality, industry-standard qubit platform suitable for

quantum computing applications, using this promising technology [15], it is crucial to reduce the quantum dot occupancy down to the single-electron level. In this paper, we demonstrate our numerical computations using the 3D Quantum Technology Computer Aided Design (QTCAD) simulation tool at 1.4 K along with experimental observations. Together, these computations and observations shed light on the required gate biasing and device geometry conditions to attain the single-electron regime for electronic transport tunneling through side-gate activated corner quantum dots in our device.

3. Industry-standard manufactured FD-SOI quantum dot device

The quantum dot structure developed and studied in this work is based on a modification of a conventional NMOS using the 28 nm UTBB FD-SOI technology node of STMicroelectronics [16]. Fig. 1 (a) shows a TEM image of a typical 28 nm UTBB FD-SOI MOSFET consisting of four terminals: the source, drain, gate, and back plane. The latter can be used as a second gate, usually denoted back gate, thanks to an ultra-thin 25-nm layer of Buried OXide (BOX). When the gates are polarized appropriately, electrical current flows between the source and drain of the transistor through the undoped ultra-thin 10-nm silicon film serving as the conduction channel. A unique characteristic of FD-SOI is that the thin buried insulator layer allows additional electrostatic control over the silicon channel, thus providing the ability to dynamically modulate the threshold voltage of the transistor and achieve the best trade-off between performance and power consumption.

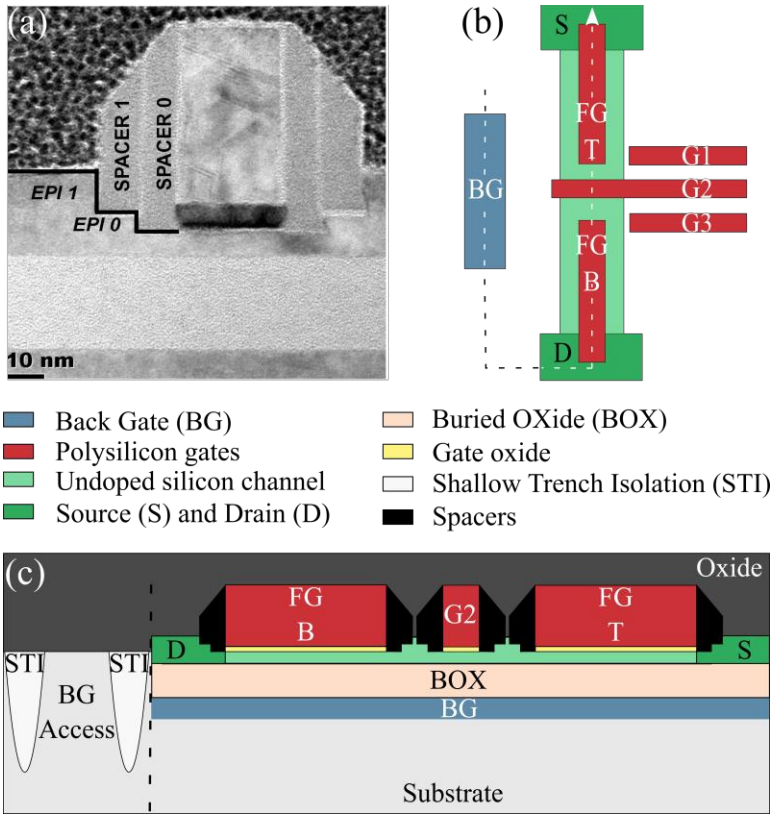

Figure 1: (a) TEM image showing the cross section of a typical 28 nm UTBB FD-SOI MOSFET fabricated in STMicroelectronics. The two spacers and epitaxial layers are indicated on the transistor. Image taken from [16]. (b) Top view schematic of the 28 nm FD-SOI split-gate device fabricated utilizing mass-production techniques. (c) Transverse cross section schematic of the 28 nm FD-SOI split-gate device following the direction indicated by the dashed line presented in the top view.

The design of our device is based on the split-gate architecture [17] and is fabricated using the thick-gate-oxide Regular V_{th} option of the 28 nm STMicroelectronics FD-SOI technology utilizing standard-process manufacturing techniques. As illustrated in Fig. 1 (b) and (c), the n-doped source and drain are epitaxially grown to decrease the series resistance thanks to the use of spacers which also serve as a protective mask for the undoped channel during the source and drain implantation. The top gates are mainly composed of polysilicon and are formed on top of a high-k gate oxide layer (shown in yellow) in the case of fabrication above the silicon channel. Otherwise, they are fabricated on top of the field oxide surrounding the device (shown in dark grey). Shallow Trench Isolation (STI) trenches filled with oxide isolate the structure from the rest of the substrate and allow electrical contact to the p-doped back plane. Therefore, due to the full dielectric isolation by the STI and BOX, the conduction channel remains undoped, thereby reducing power consumption and temperature dependence, while eliminating current leakage from and to other regions of the device. The front-end CMOS fabrication process ends with the formation of metal silicide on top of the gates, source, and drain regions, excluding the area over the channel where the quantum dot is expected to be formed.

The split-gate device was designed for conducting quantum dot transport measurements. In this context, the gate G2 splits the front gate into the two parts Front Gate Top (FGT) and Front Gate Bottom (FGB) and was designed to control the quantum dot confinement potential in the conduction channel. The exact distance between the individual gates follows STMicroelectronics' industry-standard design rules. Then, a two-dimensional electron gas (2DEG) is formed at the interface between the channel and the gate oxide giving rise to the source and drain reservoirs by applying a positive voltage on FGT and FGB respectively. The splitting between the two front gate parts leads to the formation of tunnel barriers between the electron reservoirs and quantum dot and the two lateral gates G1 and G3 were initially designed to provide additional control over their heights and widths. In this work we will see that, instead, these gates can be exploited to define side-gate activated corner dots at the interface of the channel and the field oxide.

4. Cryogenic temperature Quantum Technology Computer Aided Design simulation tool

The quantum dot device presented here was modeled in 3D using the QTCAD simulation tool [18, 19] developed by Nanoacademic Technologies Inc. This finite-element modeling (FEM) software permits the simulation of the electrical and quantum performance of the nanostructure at cryogenic temperatures.

In this work, the FEM mesh generating tool Gmsh [20] was used to define the 3D geometry of the quantum dot structure producing a first-order mesh containing 2.5 million nodes. Local mesh refinements were manually implemented in areas of fast potential variations allowing to improve precision and convergence. The various materials and regions were then specified, followed by the electrodes and the structure doping profile. Fig. 2 shows the resulting 3D computer-aided design (CAD) model without displaying the mesh. A uniform temperature of 1.4 K was imposed throughout the device which set isothermal conditions during all simulations. The following Dirichlet boundary conditions on the electrostatic potential were considered: gate (metal-insulator) boundary conditions were imposed at the polysilicon gates (surfaces shown in red color in Fig. 2) and Ohmic contacts were considered at the source and drain (surfaces shown in dark green in Fig. 2), and bottom of the BOX (bottom surface in Fig. 2). The Niagara cluster of Compute Canada was used to carry out all numerical calculations [21].

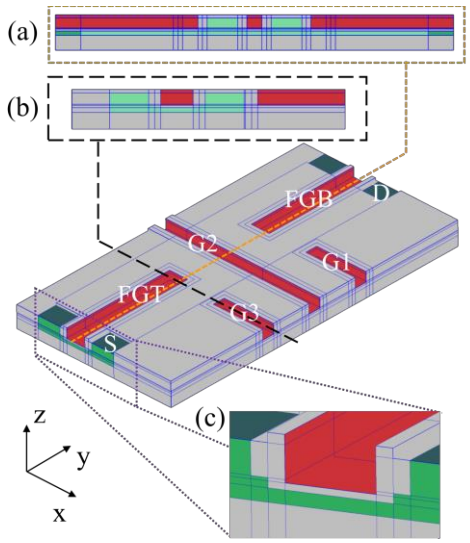

Figure 2: 3D model of the FD-SOI nanostructure based on the layout used for the actual fabrication of the device via Gmsh [20] and the QTCAD software. The device is used to form electrostatically defined quantum dots under the electrodes for quantum computing applications. (a) Transverse cross-section along the y-axis showing the two parts of the front gate (in red color), the G2 gate (in red color), and the silicon channel (in pale green color) located above the BOX (in gray color). (b) Transverse cross-section along the x-axis showing the channel, the front gate located on the silicon film and the G3 gate located on the oxide. (c) Transverse cross section along the x-axis presenting the channel, epitaxially grown source and drain, spacers, metal gate stack and, finally, the high-k gate oxide. The darkest green color denotes the surfaces to which Ohmic boundary conditions are applied in the simulations.

Considering thermodynamic equilibrium throughout the device, the non-linear Poisson equation [22, 23] is solved self-consistently, providing the electrostatic potential and the corresponding classical charge distribution according to the statistical physics of semiconductors. Explicit expressions for the Poisson equation, the charge densities, and the relationship between the band edges and the electric potential used in this work are given in [19]. In Fig. 3, a linecut of the calculated conduction band edge E_C is presented taken along the y-direction (see Fig. 2), 0.1 nm above the BOX, for various V_{G2} and V_{BG} values.

Although the formation of a single electrostatic quantum dot under the gate G2 was not observed experimentally, this gate can be exploited to regulate the tunnel barrier when the back gate is polarized appropriately to activate the conduction channel with the rest of the gates grounded, as shown by the numerical

results in Fig. 3 (b). In this paper, we show that experimental data demonstrating channel activation is well explained by QTCAD simulations at 1.4 K.

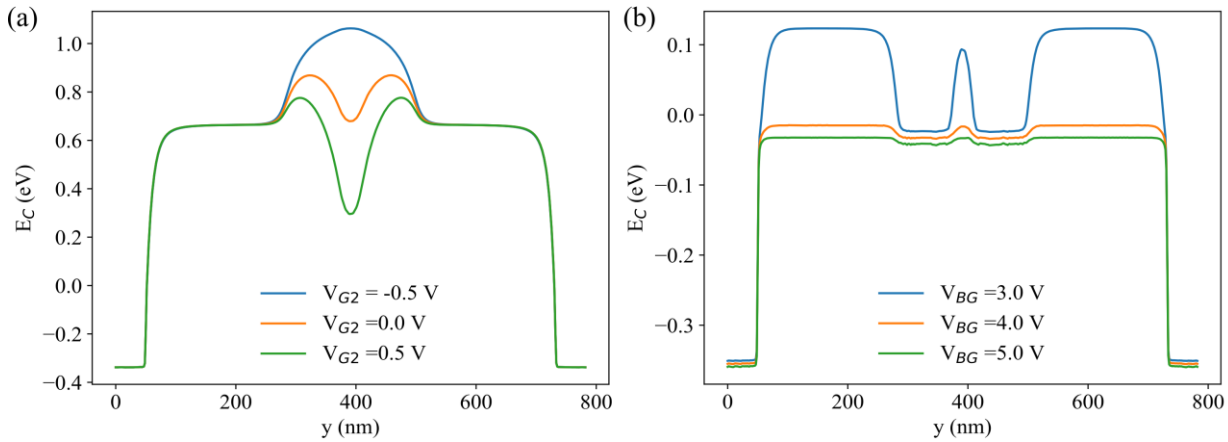

Figure 3: Estimated conduction band profile using QTCAD to solve the non-linear Poisson equation at 1.4 K. The linecuts presented here were acquired at 0.1 nm above the BOX and in the silicon film along the y-axis in the middle of the front gate (see Fig. 2). A 2DEG is observed at the Si/SiO_2 interface, as well as the ability to adjust the height of the potential barrier by applying the appropriate voltages to G2 and the back gate. The zero of E_C is equivalent to the Fermi level. (a) A voltage sweep is performed on the G2 gate while all other gates are grounded. (b) A voltage sweep is performed on the back gate while all other gates are grounded.

Specifically, the transport current flowing through the channel was measured for a voltage sweep, and a voltage step performed on the G2 gate and the back gate respectively. The measurement results are presented in the diagram in Fig. 4, in which two regimes can be identified. In the first regime, located in the region above the black dashed line, for higher values of V_{G2}, a conduction channel is formed in the device by biasing the back gate alone. In the second regime, below this black line, the G2 gate serves as a tunnel barrier requiring the application of a voltage on the back gate to overcome it and to activate transport. Moreover, it is noticeable that an increase in the voltage applied on the back gate leads to a decrease in this tunnel barrier inducing transport for lower values of V_{G2}.

The QTCAD simulations, represented by the red and blue dots in Fig. 4, are in good agreement with the experimentally observed performance of the device. Indeed, the slope of the oblique line marking the distinct regions of activated and blocked transport is almost identical in the calculations and the measurements. In order to compare the two slopes, the numerical data have been shifted compared to the experimental results so that the two corner turn-on points, indicated by a white circle in Fig. 4, overlap. This stems from the fact that the numerical model does not consider surface charges trapped at the gate oxide interfaces, resulting in an offset between the simulated and the measured corner turn-on point. In effect, these offsets can potentially be used to assess the magnitude of the charge trap density.

Finally, it is worth noting that manual optimization of the mesh as done here was a preliminary step in the development of QTCAD. It was indeed found that convergence properties of the non-linear Poisson equation depend dramatically on the mesh density in regions where the conduction band edge crosses the Fermi level. The location of these regions cannot easily be predicted and may vary with gate bias configurations. Manual meshing thus imposed a significant time overhead to the user, and typically led to excessive node number. To alleviate this burden in future simulations, an automatic adaptive meshing scheme that systematically enables convergence at temperatures down to 100 mK was recently implemented [19].

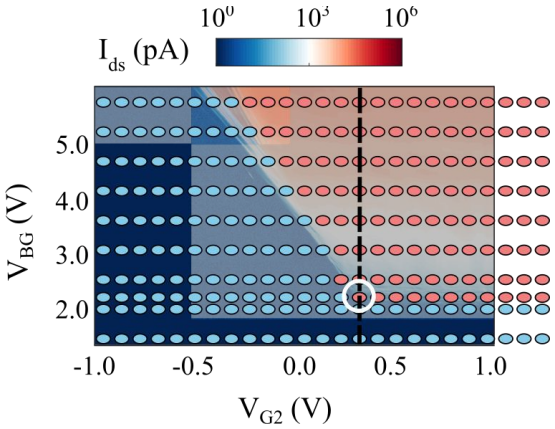

Figure 4: Comparison between theoretical computations using QTCAD and experimental measurements of current flowing through the conduction channel versus V_{BG} and V_{G2} at 1.4 K. The black dashed line separates the diagram into two regions demonstrating two different regimes of channel activation in the device. Density plot: experimentally measured current for a non-activated (blue region) and activated (red region) channel. In the dark blue region, we have set artificially the current to zero to reduce the measurement time. Blue dots: numerical calculations of the band diagram estimating blocked transport. Red dots: numerical calculations estimating allowed transport. In the characterized structure, a corner turn-on point is observed at (V_{G2}, V_{BG}) = (0.34, 2.24) V (white circle). In the modeled device, it is observed at (V_{G2}, V_{BG}) = (0.0, 3.7) V. The numerical data have been shifted in the V_{G2} and V_{BG} axes by 0.34V and -1.46V, respectively, so that these two turn-on points fit together revealing an almost identical slope of the inclined line separating the discrete regions of activated and blocked transport in theory and experiment.

5. Appearance of side-gate activated corner dots in the FD-SOI split-gate device

We will present here numerical results based on the modeling and the measurement of the fabricated device showing that side-gate activated corner quantum dots [24] can be formed in front of G1 and G3 when a positive bias is applied to these lateral gates.

With zero bias on the back gate, the large spacing between the FGT, G2 and FGB gates leads to large tunnel barriers and thus does not allow transport to be measured experimentally without surpassing the nominal supply voltage of the polysilicon gates (1.8 V) and generating a substantial leakage current flowing between the gates and the channel. Nevertheless, since the distance of G1 and G3 from the channel is larger than for G2, it is possible to bias these gates with voltages much higher than 1.8 V before the induced leakage current towards the channel causes a problem. Therefore, the additional potential induced by a voltage in the order of 10 V applied to G1 and G3 brings the conduction band under the Fermi level and forms a conduction channel. Reference [25] reports current measurements in the Coulomb blockade regime as a function of the V_{G1} and V_{G3} biases which enabled a triangulation analysis suggesting the formation of quantum dots near G1 and G3 (Fig. 5 (a)).

While the triangulation technique is described in Reference [25], we summarize it here for completeness. After collecting current measurement for each pair of electrode potentials (among FGT, FGB, G1, G2, and G3), the relative slope of transitions in each charge stability diagram was extracted. In the double-dot charge stability diagram for each electrode pair, along a line parallel to a charge transition, the quantum dot charge is constant, giving:

$$\Delta Q = C_i \Delta V_i + C_j \Delta V_j = 0, \quad (1)$$

which results in:

$$\alpha = \frac{C_i}{C_j} = -\frac{\Delta V_j}{\Delta V_i},$$

(2)

where α is the relative lever arm of gate i with respect to gate j, $\Delta V_{i,j}$ the variations in gate voltage in a transition, and $C_{i,j}$ the gate capacitances.

In parallel, a simple approximate electrostatic model was used in Ref. [25] to calculate the electrostatic potential in a 2D model of the device, without taking into account the shielding effects, quantum confinement and 3D geometry of the active region and the gates [35]. For each pair of gates, this model enabled to identify curves in space (called equi-lever arm curves) along which gate bias increments lead to a change in potential that is equal to the measured lever arm ratio. The regions with the same ratio $\alpha_{theo} = \alpha_{exp}$ are shown in Fig. 5 (a). An uncertainty of ±30% is identified nevertheless to these lever-arm curves, considering the inaccuracy of the theoretical model and of the extraction of the relative lever arms. The regions that maximize the number of overlaps between the equi-lever arm curves (shown in blue in Fig. 5(a)) indicate that the most probable location of the quantum dots is between the gates G1-FGT and G3-FGB on both sides of the G2 gate.

QTCAD simulations predict the formation of side-gate activated corner dots at positions that are compatible with the results of the analysis performed on the experimental data. More precisely, Fig. 5 (b) shows the numerically calculated conduction band edge profile over a slice along the x-y plane, 1 nm below the interface between the channel and the gate oxides, displaying clear energy-potential minima in front of G1 and G3. Since the conduction band edge acts as a confinement potential energy for conduction electrons, we investigate the existence of bound states in these minima by numerically solving the time-independent single-electron effective-mass Schrödinger's equation

$$V(\mathbf{r})F(\mathbf{r}) - \frac{\hbar^2}{2}\nabla \cdot [\mathbf{M}_e^{-1} \cdot \nabla F(\mathbf{r})] = \epsilon\, F(\mathbf{r}),$$

(3)

where $V(\mathbf{r}) \equiv E_C$ is the electron confinement potential and $\mathbf{M}_e^{-1}$ is the inverse effective mass tensor. Eigenenergies and eigenfunctions (envelope functions) of this equation are given by ϵ and $F(\mathbf{r})$, respectively. Assuming that the valley degeneracy is completely lifted by strong quantum confinement along the z-direction and by the sharp band-edge discontinuity at the silicon/oxide interface [26, 27, 28], we use the inverse effective mass tensor corresponding to the $\pm\hat{\mathbf{z}}$ valleys: $\left[\left[\frac{1}{m_t}, 0, 0\right], \left[0, \frac{1}{m_t}, 0\right], \left[0, 0, \frac{1}{m_l}\right]\right]$, where $m_t = 0.19m_e$ and $m_l = 0.916m_e$ are the transverse and longitudinal silicon effective masses, respectively. The numerical solution of Eq. (3) resulted in bound eigenstates localized near the top edge of the channel in front of G1 and G3 (Fig. 5 (c)), thus corroborating the experimental evidence of side-gate activated corner dots at these areas. We also note that the back gate provides an additional tuning opportunity as it can be used to tune the distance between the wavefunctions and the interfaces to either enhance the valley splitting or protect the quantum-confined electron from defects.

Although other studies have reported the demonstration of corner dots in purely R&D FD-SOI structures that do not comply with industrial manufacturing processes ([36], [37]) , we present for the first time in this paper the formation of side-gate activated corner dots hosted in a nanostructure fabricated using the industry-standard 28 nm FD-SOI process. Given the potential of such corner dots for all-electrical manipulation of spin qubits thanks to independently tunable spin-valley mixing and quantum confinement [37], it becomes

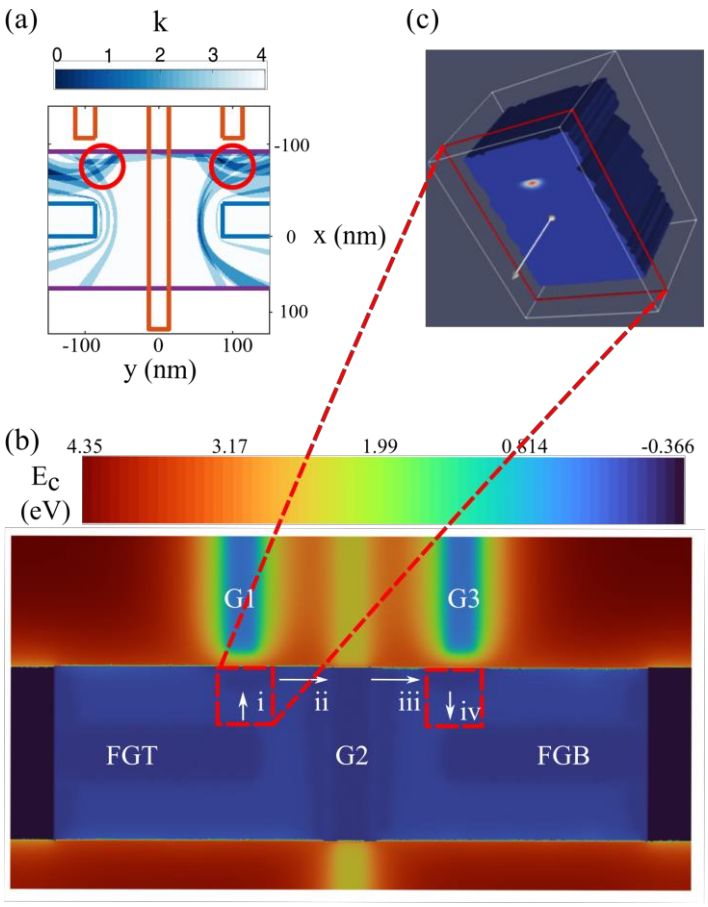

Figure 5: Numerical simulations based on the modeling and the measurement of the fabricated device Experimental evidence and numerical indicating the presence of side-gate activated corner dots near G1 and G3. Fixed voltages are applied to the gates: $V_{G1} = V_{G3} = 4\,V, V_{FGT} = V_{FGB} = 843\,mV, V_{BG} = 0\,V, V_{G2} = 1.7\,V$ (a) Lever arm analysis which allowed to estimate the position of the two quantum dots using an electrostatic triangulation technique. Every equi-lever-arm area (shown in blue) corresponds to the condition $\alpha_{theo} = \alpha_{exp} \pm 30\%$ for a single pair of V_{G1} and V_{G3} biases, where α_{theo} was calculated using a coarse electrostatic model (see main text) and α_{exp} was extracted from experimental charge stability diagrams. The most probable quantum-dot locations are at the intersection of equi-lever arm areas. The color scale represents the number of these intersections, k. (b) Numerical calculation of the conduction band edge using QTCAD. The arrows and roman numerals indicate the sequential tunneling transport model employed in the simulations discussed in Section 6. (c) Numerical calculation of the ground state of single electrons in front of G1 using QTCAD.

important and non-trivial to understand the conditions necessary to achieve single-electron occupancy of these quantum dots. This can be quantitatively accomplished effectively using TCAD simulations, as these conditions strongly depend on the interplay of charge energies and tunnel barriers which are determined by the geometry of the system, material properties and applied potentials.

6. Coulomb blockade simulations in the FD-SOI split-gate device

To investigate the transport mechanism based on electron tunneling through the two side-gate activated corner dots studied in Section 5, we compared sequential tunneling simulations using QTCAD's many-body and master equation solvers to transport measurement results. The theoretical framework of these many-body transport simulations is introduced in Appendix A, below.

Based on experimental observation, a transport model was postulated in which an electron sequentially undergoes the tunneling events that follow: (i) tunneling from the source reservoir (below gate FGT) to the dot QD1 (in front of G1), (ii) tunneling from QD1 to the 2DEG island created under G2, (iii) tunneling from the island below G2 to QD3 (in front of G3), (iv) tunneling from QD3 to the drain reservoir (below gate FGB) (see Fig. 5 (b)). Because of the depth and width of the corresponding potential well (see Fig. 5 (b)), the region below G2 behaves more like an additional electron reservoir (akin to the source and drain) than as a quantum dot.

Fig. 6 (a) shows experimental measurements of a charge stability diagram at strong $V_{G1} = V_{G3}$ biases near 10 V [25]. The width of the Coulomb diamonds along the V_{SD} axis indicates a charging energy of ~ 5 meV that is almost independent of $V_{G1} = V_{G3}$, suggesting that the uncoupled quantum dots formed in front of G1 and G3 are both in the many-electron regime under these bias conditions. Importantly, for these quantum dots, the single-electron regime was never observed experimentally. Because quantum computing applications typically require single electrons, we use QTCAD to investigate conditions for the single electron regime to be achieved. To do so, we consider a simplified scenario in which transport may be modeled separately for a single quantum dot. Choosing QD1 as this single quantum dot, the source corresponds to the region below FGT, while the 2DEG below G2, QD3, and the region below FGB are modeled as a single effective drain. To investigate the onset of the single electron regime, we first diagonalize the many-body Hamiltonian, Eq. (A 2), using the first $n_{states} = 3$ eigensolutions of Eq. (3) as a spin-degenerate set of basis states. Using the resulting many-body eigenenergies, we find the quantum dot chemical potentials through their definition [32]

$$\mu(N) = E_{tot}(N) - E_{tot}(N-1), \tag{4}$$

where $E_{tot}(N)$ is the total energy of the system in its N-electron ground state. For QD1, we find the chemical potentials {-0.416 -0.387 -0.351 -0.327 -0.292 -0.272} eV, leading to charging energies whose order of magnitude is comparable to experimental observation in the many-electron regime (5-10 meV). The electrical configuration on the simulated device was the following: $V_{G1} = V_{G3} = 4\,V$, $V_{G2} = 1.7\,V$, $V_{FGT} = V_{FGB} = 843\,mV$, and $V_{BG} = 0\,V$.

The single-electron regime is achieved when only the chemical potential $\mu(1)$ lies below the Fermi energy set by the source and drain. To find the gate bias V_{G1} that leads to this single-electron regime, it is necessary to compute the lever arm α of this gate over the quantum dot, defined as the conversion factor between V_{G1} and the chemical potentials of the quantum dot [33]

$$\mu(N) = \mu_0(N) - q\alpha(V_{G1} - V_{ref}), \tag{5}$$

where μ_0 is the dot chemical potential with $V_{G1} = V_{ref} = 4V, with\ V_{ref}$ being a reference G1 bias, and where we have assumed linear behavior with respect to gate bias, and a single lever arm α, for all chemical potentials of interest. Taking $N = 1$, we calculate α by computing the single-electron ground energy of QD1 as a function of V_{G1} by successively solving the non-linear Poisson and Schrödinger's equation and taking a linear fit. Fig. 7 shows the estimated single-electron energy spectrum of QD1, presenting different energy states as a function of the V_{G1} bias (solid color lines). The linear regression to the ground-state energy is also plotted in the figure (dashed black line), which gives $\alpha = 0.2\ eV/V$. Using this lever arm, we find the position of the

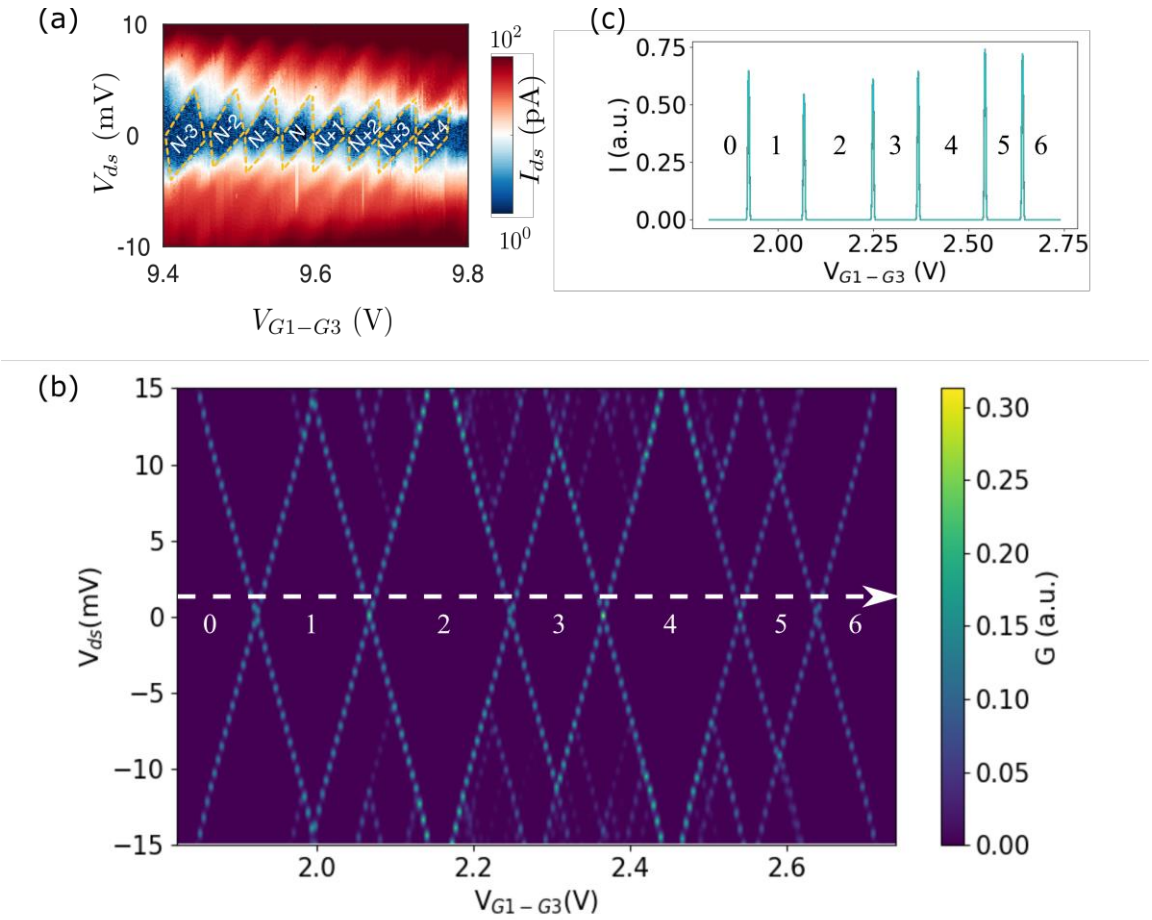

Figure 6: Comparison between numerical calculations and experimental measurements of Coulomb blockade spectroscopy performed on the split-gate device at 1.4 K. The parameters of the electrical configuration of the device are the following: $V_{FGT} = V_{FGB} = 843\ mV$, $V_{G2} = 1.7\ V$, and $V_{BG} = 0\ V$. (a) Measured Coulomb diamonds corresponding to QD1 as a function of the V_{G1-G3} voltage indicating a charging energy E_C of approximately 5-10 meV corresponding to a single quantum dot in the large-electron number regime. (b) Calculated Coulomb diamonds corresponding to QD1 using QTCAD. (c) Coulomb blockade oscillations estimated using QTCAD for a low bias of $V_{ds} = 1\ mV$ as a function of the V_{G1-G3} voltage applied simultaneously to the lateral gates G1 and G3, corresponding to the single quantum dot QD1.

Coulomb peaks by solving for V_{G1} in Eq. (5) for each value of N. For the current structure, these Coulomb peak positions are {1.92, 2.07, 2.25, 2.37, 2.54, 2.64} V.

Beyond peak positions, in this idealized single-dot scenario, we may solve the master equation, Eq. (A 9) for sequential tunneling through G1 and extract a current. The tunneling rates appearing in this master equation depend on the broadening function (see Appendix A), which we set to an arbitrary constant value. Despite not giving us the absolute value of the current, this approach still allows us to compute Coulomb peak shapes, their relative height, and the overarching charge stability diagram.

Fig. 6 (b) presents the numerical calculation of the Coulomb blockade diamonds displaying the differential conductance, resulting from the solution of the master equation at 1.4 K. The fact that the even-numbered simulated diamonds appear to be larger than the odd-numbered ones is consistent with well-established predictions of artificial-atom physics [34]. Indeed, the widths of the diamonds are proportional to the addition energies of the artificial atom formed by the quantum dot. For 2D quantum dots, higher addition energies are

expected for N=2 and 6, i.e., at magic numbers of a two-dimensional circular harmonic potential. Such magic numbers correspond to the filling of atomic shells. The addition energy for N=4 is also expected to be enhanced due to half filling of the second atomic shell according to Hund's rule.

Fig. 6 (c) illustrates the estimated current at a V_{ds} bias of 1 mV (corresponding to the horizontal dashed white line in Fig. 6 (b)). The position of the peaks displayed in Fig. 6 (c) matches the calculation described above based on the dot chemical potentials and lever arm, allowing us to associate Coulomb diamonds and spacings between peaks to bias configurations leading to N electrons occupying the quantum dot. From this analysis, the single-electron regime is achieved for QD1 at $V_{G1} \approx 2$ V.

Studying the tunnel barriers formed between the quantum dots and the electron reservoirs (Fig. 8) permitted us to gain useful insights into experimental conditions required to achieve the single-electron regime. Although a single electron may in principle be loaded onto the side-gate activated corner dots in front of G1 and G3 for sufficiently low gate bias, the tunnel barriers between the dots and reservoirs are too high (roughly

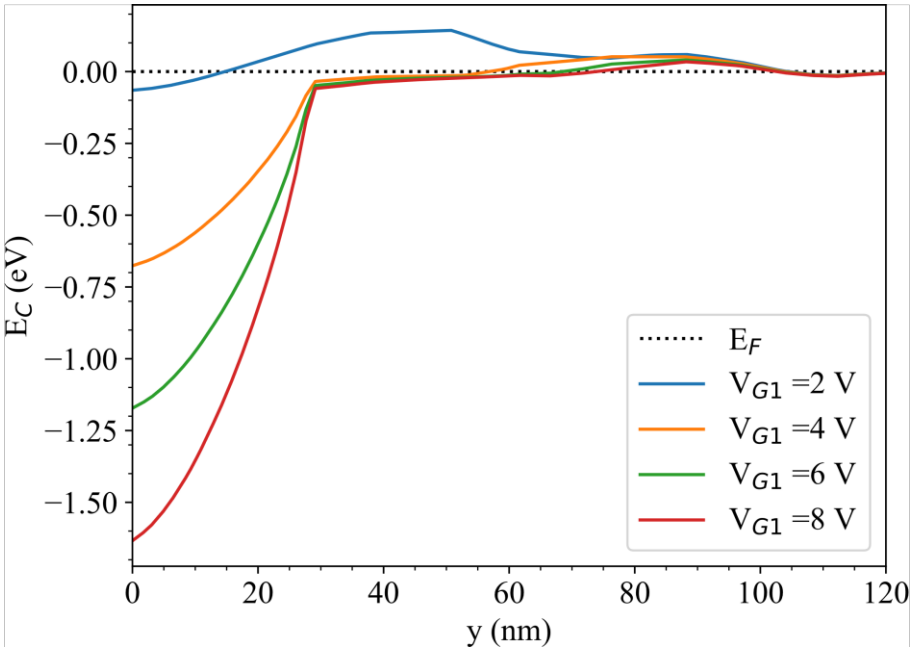

Figure 8: Estimated conduction band profile using QTCAD at 1.4 K. The linecuts presented here were acquired at 0.1 nm below the top gate oxide, in the silicon film along the white arrow (ii) in Fig. 5 (b). The ability to adjust the height of the potential barrier by modifying the V_{G1} bias is observed. The zero of E_C corresponds to the Fermi level. The parameters of the electrical configuration of the device are the following: $V_{FGT} = V_{FGB} = 843\ mV$, $V_{G2} = 1.7\ V$, and $V_{BG} = 0\ V$.

100 meV) and too wide (roughly 50 nm) to allow transport current to be measured (see, e.g., the blue line in Fig. 8). Consequently, the single-electron regime could not be observed at the experimental gate bias of 2 V at which the single-electron regime is expected from the simulations. In contrast, for large gate biases, simulations show that the barrier heights and widths may be dramatically reduced (see, e.g., the red line in Fig. 8). However, such biases would lead to many electrons being loaded into the device, consistent with experimental observations.

7. Conclusions

We presented our work on the simulation of a 28 nm FD-SOI standard-process quantum dot device at cryogenic temperatures using the QTCAD simulation tool. Electrostatic calculations performed at 1.4 K

confirmed the experimental observation of channel activation by the coordinated operation of the G2 and back gate. Furthermore, effective-mass Schrödinger computations validated the experimental evidence indicating the formation of quantum dots in front of the G1 and G3 gates and elucidated their side-gate activated corner dot nature. Last, transport simulations clarified the reason why the single-electron regime was not observed experimentally for these dots indicating that narrower and lower potential barriers are required. These results provide an essential insight into the transport mechanisms occurring in the split-gate device and the requirements on gate bias and device geometry conditions to overcome the observed limitations, thus paving the way towards the realization of a next generation of FD-SOI quantum dot devices with reduced critical dimensions.

Appendix A: Many-body theory of sequential tunneling in a quantum dot

In this Appendix, we provide theoretical background for the many-body and out-of-equilibrium statistical physics of transport in a quantum-dot system and describe the equations that are solved in Section 6 to calculate properties of the current flowing through the quantum dot near G1.

To model transport, we consider a quantum dot connected to two leads: the source and the drain. While the quantum dot is modeled using finite elements, the source and the drain are not explicitly related to any region of the CAD model – we only assume that they are coupled to the quantum dot through the total Hamiltonian

$$H = H_D + H_{DR} + H_R, \tag{A 1}$$

where H_D is the Hamiltonian of the quantum dot, H_R is the Hamiltonian of the electron reservoir formed by the source and drain, and H_{DR} is the Hamiltonian that couples the quantum dot and the reservoir. In second quantization, these Hamiltonians are given by [29]

$$H_D = \sum_{i\sigma} \epsilon_{i\sigma} c_{i\sigma}^\dagger c_{i\sigma} + \frac{1}{2} \sum_{ijkl,\sigma\sigma'} V_{ijlk} c_{i\sigma}^\dagger c_{j\sigma'}^\dagger c_{k\sigma'} c_{l\sigma}, \tag{A 2}$$

$$H_R = \sum_{\mathbf{k}L\sigma} \epsilon_{\mathbf{k}L} c_{\mathbf{k}L}^\dagger c_{\mathbf{k}L}, \tag{A 3}$$

$$H_{DR} = \sum_{\mathbf{k},L,i,\sigma} \left(t_{\mathbf{k}L,i\sigma}^* c_{\mathbf{k}L}^\dagger c_{i\sigma} + \text{H. c.} \right). \tag{A 4}$$

In the above equations, we have introduced the fermionic operator c_a that destroys an electron in the state labeled by a: a collective index that simultaneously labels all degrees of freedom (DOF) of an electron in the quantum dot or in one of the leads. For the quantum dot, these DOF are single-electron orbital and spin indices: $a \to i\sigma$. For the leads, these DOF are the wavevector $\mathbf{k}$ and the lead index L (either S for source or D for drain): $a \to \mathbf{k}L$.

In Eq. (A 2), we have introduced the single-electron energies $\epsilon_{i\sigma}$ and the matrix elements of the Coulomb interaction

$$V_{ijkl} = \int d\mathbf{r}_1 \int d\mathbf{r}_2 \, F_i^*(\mathbf{r}_1) F_j^*(\mathbf{r}_2) \frac{q^2}{4\pi\varepsilon|\mathbf{r_1} - \mathbf{r_2}|} F_k(\mathbf{r_1}) F_l(\mathbf{r_2}),$$

(A 5)

where $F_i(\mathbf{r})$ is the i-th single-electron envelope function, ε is the dielectric permittivity, and integration is done over all space. We note that $\epsilon_{i\sigma}$ and $F_i(\mathbf{r})$ are simply the eigenenergies and eigenfunctions of the single-electron effective Schrödinger's equation, Eq. (3). In addition, while Eq. (3) captures only the orbital DOF of an electron, here we neglect Zeeman splitting and enforce a two-fold spin degeneracy for each single-electron eigenstate, i.e., $\epsilon_{i\uparrow} = \epsilon_{i\downarrow} = \epsilon_i$, with ϵ_i being the i-th eigenenergy of Eq. (3) and $\uparrow$ ($\downarrow$) labeling spin up (down) states.

Finally, in Eqs. (A 3) and (A 4), we have also introduced $\epsilon_{\mathbf{k}L}$, the energy of a reservoir electron eigenstate labeled by $\mathbf{k}L$, and $t_{\mathbf{k}L,i\sigma}$, the tunneling matrix element between the $i\sigma$ and the $\mathbf{k}L$ single-electron eigenstates of the quantum dot and lead L, respectively.

To model transport through the quantum dot, we treat coupling to the electron reservoir as a weak perturbation. Within the $2n_{\text{states}}$-dimensional truncated spin-degenerate basis set $\{F_i(\mathbf{r})\}, i \in \{1,2,\dots,n_{\text{states}}\}$, we perform exact diagonalization of the quantum-dot many-body Hamiltonian H_D [30]. Since the many-body Hamiltonian preserves the total number of electrons N, H_D is block-diagonal in any basis that commutes with this quantum number. Diagonalizing block by block, we write the α-th many-body eigenenergy and eigenstate of the N-electron subspace as E_α^N and $|\,\alpha_N\rangle$, respectively. Within first-order perturbation theory, coupling of the quantum dot to the source and drain through H_{DR} then leads to transitions of the form $\alpha_N \to \beta_{N+1}$ or $\alpha_N \to \beta_{N-1}$, i.e., between many-body eigenstates from subspaces that differ by one electron. These transitions occur at rates $\Gamma^L(\alpha_N \to \beta_{N+1})$ and $\Gamma^L(\alpha_N \to \beta_{N-1})$ for lead L. From Fermi's Golden Rule, these transition rates are given by [29]

$$\Gamma^L(\alpha_N \to \beta_{N+1}) = n_F\big(E_\beta^{N+1} - E_\alpha^N - E_F^L\big) \sum_{ij\sigma\sigma'} \langle\beta_{N+1}|c_{i\sigma}^\dagger|\alpha_N\rangle \Gamma_{i\sigma j\sigma'}^L \big(E_\beta^{N+1} - E_\alpha^N\big) \langle\alpha_N|c_{j\sigma'}|\beta_{N+1}\rangle,$$

(A 6)

$$\Gamma^L(\alpha_N \to \beta_{N-1}) = \big[1 - n_F\big(E_\alpha^N - E_\beta^{N-1} - E_F^L\big)\big] \sum_{ij\sigma\sigma'} \langle\alpha_N|c_{i\sigma}^\dagger|\beta_{N-1}\rangle \Gamma_{i\sigma j\sigma'}^L \big(E_\alpha^N - E_\beta^{N-1}\big) \langle\beta_{N-1}|c_{j\sigma'}|\alpha_N\rangle,$$

(A 7)

where $n_F(E) = 1/[1 + e^{E/k_BT}]$ is the Fermi-Dirac distribution, E_F^L is the Fermi energy of lead L, k_B is the Boltzmann constant, T is the electron temperature, and where we have introduced the broadening function

$$\Gamma_{i\sigma j\sigma'}^L(E) = \frac{2\pi}{\hbar} \sum_{\mathbf{k}L} t_{\mathbf{k}L,i\sigma}^* \, t_{\mathbf{k}L,j\sigma'} \delta(E - \epsilon_{\mathbf{k}L}).$$

(A 8)

In this equation, the tunneling matrix elements $t_{\mathbf{k}L,i\sigma}$ are typically unknown. In addition, the broadening function ultimately depends on the density of reservoir states at energy E. Assuming that this density of states is approximately constant over the 1-10 meV energy scale considered here (set by the source-drain bias), and that the tunneling matrix elements are also nearly independent of energy and spin, we approximate the

broadening function by a single constant Γ_0. Though the value of this constant is unknown, this approach still allows us to compute the shape and relative height of Coulomb peaks and obtain charge stability diagrams.

As made explicit in Eqs. (A 6) and (A 7), in the above first-order approach, only transitions that exchange a single electron between the quantum dot and one of the leads are allowed, corresponding to the sequential tunneling regime. In other words, we neglect co-tunneling events that arise at higher order in perturbation theory [31].

Also neglecting coherence effects, we describe transport through the quantum dot using the master equation [29]

$$\frac{dp_m}{dt} = -p_m \sum_{n \neq m} \gamma_{nm} + \sum_{n \neq m} p_n \gamma_{mn} = 0, \tag{A 9}$$

$$\gamma_{mn} = \Gamma^S(n \to m) + \Gamma^D(n \to m), \tag{A 10}$$

where m and n are indices that span all the many-body eigenstates α_N of H_D. Evidently, within the first order approach described above, $\Gamma^L(n \to m) \neq 0$ if and only if n and m are within subspaces that differ by one electron. In the approach described here, the non-equilibrium statistics of the quantum-dot is captured by the collection of occupancy probabilities p_m. Assuming steady-state behavior, we set the time derivative of each p_m to zero in the master equation [see the second equality in Eq. (A 9)], which then reduces to a system of linear equations which is easily solved numerically. The current arising from electrons entering the quantum dot from the source is then given by

$$I^S = -e \sum_{\alpha\beta,N} p_{\alpha_N} [\Gamma^S(\alpha_N \to \beta_{N+1}) - \Gamma^S(\alpha_N \to \beta_{N-1})]. \tag{A 11}$$

Also introducing the current I^D arising from electrons entering the quantum dot from the drain, we have $I^S + I^D = 0 \Rightarrow I^D = -I^S$ due to charge conservation.

Finally the differential conductance is defined in terms of the current flowing through the quantum dot as

$$G = \frac{dI^S}{dV_{ds}},$$

where $V_{SD} \equiv V_D - V_S$ is the source-drain bias. This differential conductance is plotted in Fig. 6, and allows to identify transport signatures of the single-electron regime.

Acknowledgements

The authors of this paper would like to thank all the colleagues from STMicroelectronics who contributed to the design and fabrication of the samples, and especially F. Arnaud, C. Gardin, A. Poulin, K. Tournon, N. Guitar, C. Charbuillet, and T. Bédécarrats. They would also like to thank all the colleagues from the Institut

quantique for their technical support during the experimental process, and especially M. Lacerte, C. Lupien, B. Rivard, and S. Pelletier. This work was supported by the French program Conventions Industrielles de Formation par la Recherche (CIFRE), the Canada First Research Excellence Fund (CFREF), the Natural Sciences and Engineering Research Council of Canada (NSERC), and the *Ministère de l'Économie et de l'Innovation du Québec*.

[1]D. Loss and D. P. DiVincenzo "Quantum computation with quantum dots", in *Physical Review A*, vol. 57, no. 120, 1998

[2] R. Maurand *et al.* A CMOS silicon spin qubit, *Nature Communications*, 7, 13575, 2016

[3] M. Veldhorst *et al.* Silicon CMOS architecture for a spin-based quantum computer, *Nature Communications* 8**,** 1766, 2017

[4] S.J. Pauka *et al.* A cryogenic CMOS chip for generating control signals for multiple qubits, *Nature Electronics*, 4, 64–70, 2021

[5] X. Xue *et al.* CMOS-based cryogenic control of silicon quantum circuits, *Nature* **593,** 205–210, 2021

[6] A. M. J. Zwerver *et al.* Qubits made by advanced semiconductor manufacturing, *Nature Electronics,* 5**,** 184–190, 2022

[7]L. Hutin *et al.* "SOI CMOS technology for quantum information processing", in *2017 IEEE International Conference on IC Design and Technology (ICICDT)*, pp. 1–4. IEEE, 2017

[8]E. Simoen and C. Claeys "The cryogenic operation of partially depleted silicon-on-insulator inverters", in *IEEE Transactions on Electron Devices*, vol. 42, no. 6, pp. 1100-1105, 1995

[9]P. Galy *et al.* "Cryogenic Temperature Characterization of a 28-nm FD-SOI Dedicated Structure for Advanced CMOS and Quantum Technologies Co-Integration", in *IEEE Journal of the Electron Devices Society*, vol. 6, pp. 594–600, 2018

[10] T. Wada *et al.* "Development of low power cryogenic readout integrated circuits using fully-depleted-silicon-on-insulator CMOS technology for far-infrared image sensors", in *Journal of Low Temperature Physics,* vol. 167, no. 5-6, pp. 602–608, 2012

[11] H. Bohuslavskyi *et al.* "Cryogenic subthreshold swing saturation in FD-SOI MOSFETs described with band broadening", in *IEEE Electron Device Letters*, vol. 40, pp. 784-787, 2019

[12] M. Casse *et al.* "Evidence of 2D Intersubband Scattering in Thin Film Fully Depleted Silicon-On-Insulator Transistors Operating at 4.2K ", in *Applied Physics Letters*, vol. 116, no. 24, 2020

[13] B. Cardoso Paz *et al.* "Front and back channels coupling and transport on 28 nm FD-SOI MOSFETs down to liquid-He temperature", in *Solid State Electronics Letters*, vol. 186, 2021

[14] D. Flandre *et al*. "Fully-depleted SOI CMOS technology for low-voltage low-power mixed digital/analog/microwave circuits", in *Analog Integrated Circuits and Signal Processing*, vol. 21, pp. 213–228, 1999

[15] I. Kriekouki, "Industrial approach to quantum dots in fully-depleted silicon-on-insulator devices for quantum information applications" (PhD thesis), 2022. Retrieved from https://savoirs.usherbrooke.ca/

[16] N. Planes *et al.* "28FDSOI Technology for Low-Voltage, Analog and RF applications", in *2016 13th IEEE International Conference on Solid-State and Integrated Circuit Technology (ICSICT)*, pp. 10–13. IEEE, 2016

[17] S. Rochette *et al.* "Quantum dots with split enhancement gate tunnel barrier control", in *Applied Physics Letters*, vol. 114, no. 083101, 2019

[18] https://www.nanoacademic.com/product-page/qtcad

[19] F. Beaudoin, P. Philippopoulos, C. Zhou, I. Kriekouki, M. Pioro-Ladrière, H. Guo and P. Galy, in *Applied Physics Letters*, vol. 120, no. 264001, 2022

[20] C. Geuzaine and J. F. Remacle "Gmsh: a three-dimensional finite element mesh generator with built-in pre- and post-processing facilities", in *International Journal for Numerical Methods in Engineering*, vol. 79, no. 11, pp. 1309-1331, 2009

[21] https://www.computecanada.ca/home/

[22] M. Stopa "Quantum dot self-consistent electronic structure and the Coulomb blockade", in *Physical Review B*, vol. 54, no. 13767, 1996

[23] X. Gao *et al.* "Quantum computer aided design simulation and optimization of semiconductor quantum dots", in *Journal of Applied Physics*, vol. 114, no. 164302, 2013

[24] H. Sellier *et al.* "Subthreshold channels at the edges of nanoscale triple-gate silicon transistors", in *Applied Physics Letters*, vol. 90, no. 073502, 2007

[25] J. Camirand Lemyre, "Engineering of quantum systems for scaling up to industrial microelectronics platforms" (PhD thesis), 2019. Retrieved from https://savoirs.usherbrooke.ca/

[26] A. L. Saraiva *et al*. "Physical mechanisms of interface-mediated intervalley coupling in Si", in *Physical Review B*, vol. 80, no. 081305, 2009

[27] C. Tahan and R. Joynt. "Relaxation of excited spin, orbital, and valley qubit states in ideal silicon quantum dots" in *Physical Review B*, vol. 89, no. 075302, 2014

[28] J. K. Gamble *et al*. "Valley splitting of single-electron Si MOS quantum dots" in *Applied Physics Letters*, vol. 109, no. 253101, 2016

[29] H. Bruus and K. Flensberg. *Many-body quantum theory in condensed matter physics: an introduction*. OUP Oxford, 2004

[30] D. Güçlü *et al*. "Geometric blockade in a quantum dot: Transport properties by exact diagonalization" in *Physical Review B*, vol. 66, no. 195327, 2002

[31] F. Qassemi et al. "Stationary and Transient Leakage Current in the Pauli Spin Blockade" in *Physical Review Letters*, vol. 102, no. 176806, 2009

[32] R. Hanson et al. "Spins in few-electron quantum dots" in *Reviews of Modern Physics*, vol. 79, pp. 1217-1265, 2007

[33] A. Fuhrer. "Phase coherence, orbital and spin states in quantum rings" (PhD thesis). ETH Zurich, 2003

[34] L. P. Kouwenhoven *et al*. "Few-electron quantum dots" in *Reports on Progress in Physics*, vol. 64, pp. 701-736, 2001.

[35] J. H. Davies *et al*. "Modeling the patterned two-dimensional electron gas: Electrostatics" in *Journal of Applied Physics*, vol. 77, p. 4504, 1995.

[36] A. Corna *et al*. "Electrically driven electron spin resonance mediated by spin-valley-orbit coupling in a silicon quantum dot" in *npj Quantum Information*, vo. 4, no 6, 2018.

[37] L. Bourdet and Y.-M. Niquet. "All-electrical manipulation of silicon spin qubits with tunable spin-valley mixing" in *Physical Review B*, vol. 97, no. 155433, 2018.